

Optical and magneto-optical properties of $R\text{Fe}_2$ ($R=\text{Gd},\text{Tb},\text{Ho},\text{Lu}$) and GdCo_2

S. J. Lee, R. J. Lange, P. C. Canfield, B. N. Harmon, and D. W. Lynch

Ames Laboratory and Department of Physics and Astronomy, Iowa State University, Ames, Iowa 50011

(Received 26 April 1999; revised manuscript received 10 January 2000)

The conductivity tensors of single crystals and polycrystals of $R\text{Fe}_2$ ($R=\text{Gd},\text{Tb},\text{Ho},\text{Lu}$) and GdCo_2 were determined in the visible and near UV ranges. The magneto-optical Kerr effect (MOKE) was studied at different temperatures and magnetic fields. The single-crystal data show more features and larger magnitudes in the MOKE spectrum than the polycrystalline data under the same experimental conditions. The theoretical optical conductivity tensors for these compounds were calculated using the tight-binding linear-muffin-tin orbital (TB-LMTO) method in the local spin-density approximation. The agreement between theory and experiment was poor except for LuFe_2 , in which the $4f$ shell is completely closed.

I. INTRODUCTION

The electronic, magnetic, and magneto-optical properties of rare-earth transition-metal intermetallic compounds have been investigated by many authors due to their usefulness in technical applications. Among them, the rare-earth Fe_2 ($R\text{Fe}_2$) intermetallic compounds have been attractive for their high Curie temperatures and the simple cubic Laves-phase ($C15$) crystal structure. Katayama *et al.*¹ measured the Kerr rotations of polycrystalline $R\text{Fe}_2$ ($R=\text{Gd},\text{Er},\text{Ho},\text{Dy}$, and Tb) using a null-type automatic Kerr spectrometer at room temperature with an applied magnetic field of 1.2 T. Mukimov *et al.*² measured the magneto-optical equatorial spectra of polycrystalline $R\text{Fe}_2$ ($R=\text{Gd}$, Tb , and Er) prepared by arc melting. From these, they derived the off-diagonal optical conductivities for GdFe_2 , TbFe_2 , and ErFe_2 . The magneto-optical Kerr effect (MOKE) data in the present experiments using single crystals show more features and larger magnitudes than the polycrystalline data. The reasons for this will be discussed. The theoretical calculation of the magneto-optical properties of magnetic materials requires accurate self-consistent band-structure calculations, otherwise the wrong interband transitions will predict incorrect MOKE phenomena. In this work we present calculations based on the local spin-density approximation (LSDA) to density-functional theory. For many itinerant electron systems the LSDA works very well, however, it is known to have difficulty with systems containing localized orbitals or highly correlated states. Nevertheless, a comparison between experiment and LSDA calculations may be useful in understanding the limitations of the theoretical models, and in elucidating structures in the measured spectra when the models have validity.

II. EXPERIMENT

Single crystals of GdFe_2 , TbFe_2 , HoFe_2 , LuFe_2 , and GdCo_2 were grown from the binary melts.³ This growth technique can be called a self-flux method in that no third element is used as a flux.⁴ For example, single crystals of GdCo_2 were grown as follows. A button-shaped sample of polycrystalline $\text{Gd}_{0.55}\text{Co}_{0.45}$ was prepared by arc melting under Ar on a water-cooled copper hearth. The button was packed into a Ta crucible and quartz wool was filled above

the crucible. This assembly was sealed in a quartz tube under a partial pressure of argon. The sample was heated to 1140°C and cooled from 1140 to 950°C within 2 h, then slowly cooled from 950 to 700°C over a period of 132 h. The crystal grew during the first cooling step. At 700°C , the sample was inverted and spun in a centrifuge, forcing the still-liquid flux out through the quartz wool and leaving the crystal in the crucible. The quartz wool in the crucible acts as the filter during flux removal. The sizes of the crystals of GdCo_2 are typically $2 \times 1 \times 1 \text{ mm}^3$. The surfaces of the as-grown single crystals were mirrorlike, so no further surface preparation was necessary. Other single crystals of $R\text{Fe}_2$ can be grown similarly.

GdCo_2 crystallizes in the cubic Laves phase with the rare-earth atoms arranged in the diamond structure consisting of two fcc structures displaced from each other by one-fourth of a body diagonal. The Co atoms are on sites of rhombohedral symmetry ($\bar{3}m$), in a tetrahedral arrangement with four rare-earth atoms as next-nearest neighbors. All the $R\text{Fe}_2$ compounds we measured have this structure.

Polycrystalline samples of GdFe_2 and TbFe_2 were prepared by arc melting. The surfaces of the polycrystals were polished with abrasives for the optical measurements, the final grade being a paste of $0.05\text{-}\mu\text{m}$ diameter alumina, then cleaned with acetone and methanol. Finally, the samples were dried with dry N_2 . The crystals are well-defined single phases and the lattice constants obtained from x-ray diffraction patterns are in accordance with previous published data. For the measurement of the diagonal part of the optical conductivity, rotating analyzer ellipsometry was employed. Ellipsometry is widely used to study the optical properties of various materials.⁵ The principle of ellipsometry is based on the fact that the state of polarization of light is changed on reflection. This change is directly related to the dielectric function of the reflecting material. With ellipsometry one measures the complex reflectivity ratio,

$$\rho = \frac{r_p}{r_s} = \left| \frac{r_p}{r_s} \right| e^{i\Delta} = \tan \Psi e^{i\Delta}, \quad (1)$$

where r_p, r_s are the complex amplitude reflection coefficients for p - and s -polarized light, and Ψ and Δ express the change in amplitude and phase between p and s components of polarized light reflected from a surface. Ψ and Δ are

quantities directly measurable from ellipsometry. This complex reflectivity ratio ρ is related to the dielectric function ϵ by⁶

$$\epsilon = \sin^2 \phi_o + \sin^2 \phi_o \tan^2 \phi_o \left[\frac{1 - \rho}{1 + \rho} \right], \quad (2)$$

where ϕ_o is the angle of incidence and ϵ and ρ are complex quantities. The ellipsometry measurements were done at room temperature in air without an external magnetic field. For n and k , the relative error is usually 2–3%, depending on sample size and surface quality. For the magneto-optical measurements, a magneto-optical Kerr spectrometer was employed, using the polar Kerr geometry, in which the applied magnetic field is perpendicular to the sample surface and parallel with the incident light beam. The angle of incidence was less than 4°. The reflection of light at near normal incidence by a magnetized surface can be described by the Fresnel reflection coefficients $\tilde{r}_\pm = r_\pm e^{i\Delta_\pm}$, where \pm represents right and left circularly polarized light, respectively.⁶ The definitions of Kerr rotation and ellipticity in terms of r_\pm and Δ_\pm are given by

$$\theta_K = -\frac{1}{2}(\Delta_+ - \Delta_-),$$

$$\epsilon_K = \frac{|r_+| - |r_-|}{|r_+| + |r_-|}. \quad (3)$$

An Al reference mirror is used to subtract the Faraday rotation due to the optical windows of the cryostat. It shows negligible Kerr rotation and ellipticity between 1 and 5 eV, even in high magnetic fields.⁷ Furthermore, to subtract the strain birefringence of the windows we need to measure with both (positive and negative) field directions because the strain effect in the windows is independent of magnetic-field direction. Therefore the formula used for the Kerr rotation θ_K is given by

$$\theta_K = [(\theta_S^+ - \theta_M^+) - (\theta_S^- - \theta_M^-)]/2, \quad (4)$$

where \pm are positive and negative magnetic fields, and the subscripts S and M designate the sample and reference mirror, respectively. The Kerr rotation changes sign under reversal of the applied magnetic field. The ellipticity ϵ_K is determined in the same way. Each spectrum we reported is the result of four scans taken over a period of typically 4 h. For the Kerr rotation and ellipticity, the error depends on photon energy. It is below 0.005° below 4 eV and increases to approximately 0.05° at 5.2 eV. The principles of the magneto-optical Kerr spectroscopy technique used was based on the method of Sato and co-workers.^{8,9} The MOKE spectrometer and calibration methods are described in detail in Ref. 10.

III. THEORY

In the macroscopic description of magneto-optical effects, the optical conductivity tensor and magneto-optical parameters are related by the Fresnel equations for reflection coefficients for right and left circularly polarized light. For small angles the complex Kerr rotation can be expressed in terms of the complex conductivity tensor components as¹¹

$$\Psi = \theta_K + i\epsilon_K = \frac{-\sigma_{xy}}{\sigma_{xx} \sqrt{1 + \frac{i4\pi}{\omega} \sigma_{xx}}}. \quad (5)$$

From this, we see that the magneto-optical parameters are directly related to the off-diagonal optical conductivity σ_{xy} . The relation between the measured magneto-optical parameters and the real and imaginary part of the off-diagonal optical conductivity tensor is given by

$$\sigma_{1xy} = \frac{\omega}{4\pi} (-A\theta_K + B\epsilon_K),$$

$$\sigma_{2xy} = -\frac{\omega}{4\pi} (B\theta_K + A\epsilon_K), \quad (6)$$

where

$$A = -k^3 + 3n^2k - k,$$

$$B = -n^3 + 3k^2n + n. \quad (7)$$

The experimental values of the optical constants n and k (real and imaginary parts of the complex refractive index) can be obtained from ellipsometry, and the experimental spectra of σ_{2xy} obtained from Eq. (6). These experimental spectra may be compared with the theoretical spectra from self-consistent electronic structure calculations.

For the band-structure calculation, the tight-binding linear muffin-tin orbital (TB-LMTO) method¹² based on the atomic-sphere approximation (ASA) with the inclusion of spin-orbit coupling is employed. It is well known that as the packing ratio of the crystal increases, the accuracy of the band-structure calculation improves for the TB-LMTO method. The structures of $R\text{Fe}_2$ ($R = \text{Gd}, \text{Tb}, \text{Ho}, \text{and Lu}$) and GdCo_2 are appropriate for the TB-LMTO method because they are closely packed structures with high symmetry. The 4f electrons of the rare-earth atoms are treated as valence electrons due to their important contributions to the magnetic and electronic structures of the rare-earth transition intermetallic compounds. The exchange-correlation potential has been included in the local spin-density approximation (LSDA) with the von Barth–Hedin form.¹³ The k -integrated functions have been evaluated by the tetrahedron technique with 144 k points in the irreducible Brillouin zone. Once the self-consistent potential and charge are obtained, the diagonal and off-diagonal parts of the optical conductivity can be calculated easily through Kubo's linear-response theory¹⁴ within the one-particle band theory. With this, one obtains the interband contribution to the conductivity tensor. A detailed derivation can be found in Wang's thesis.¹¹ Kubo's linear-response theory gives the following forms for the interband contribution to the conductivity tensor:

$$\tilde{\sigma}_{xx}(\omega) = \frac{ie^2}{m^2\hbar\Omega} \sum_k \sum_{n,l} f(\omega_l) [1 - f(\omega_n)] \left(\frac{|\pi_{nl}^+|^2 + |\pi_{nl}^-|^2}{2\omega_{nl}} \right) \times \left(\frac{1}{\omega - \omega_{nl} + i\epsilon} + \frac{1}{\omega + \omega_{nl} + i\epsilon} \right), \quad (8)$$

$$\tilde{\sigma}_{xy}(\omega) = \frac{e^2}{m^2 \hbar \Omega} \sum_k \sum_{n,l} f(\omega_l) [1 - f(\omega_n)] \left(\frac{|\pi_{nl}^+|^2 - |\pi_{nl}^-|^2}{2\omega_{nl}} \right) \times \left(\frac{1}{\omega - \omega_{nl} + i\epsilon} - \frac{1}{\omega + \omega_{nl} + i\epsilon} \right), \quad (9)$$

where $f(\omega)$ is the Fermi distribution function and l, n stand for the occupied and unoccupied energy band states at wave vector k , respectively. The momentum operator is expressed by

$$\vec{\pi} = \vec{p} + \frac{\hbar}{4mc^2} \vec{\sigma} \times \vec{\nabla} V \quad (10)$$

and

$$\pi_{nl}^\pm = \frac{1}{\sqrt{2}} \langle nk | \mp \pi_x + i\pi_y | nl \rangle. \quad (11)$$

$\pi_{nl}^\pm(k)$ are matrix elements for the left- and right-circularly polarized components of the momentum operator, respectively. In Eq. (10), \vec{p} is the momentum operator and $\vec{\sigma} \times \vec{\nabla} V$ represents the spin-orbit contribution to the matrix element. It is well known that in determining the magneto-optical effect the spin-orbit interaction, which lifts some of the degeneracies of the energy bands at high symmetry points or lines in k space, and the exchange splitting in magnetic materials play major roles.¹⁵ The form of spin-orbit interaction added to the one-electron Hamiltonian is

$$H_{SO} = \frac{\hbar}{8m^2 c^2 \pi} \vec{p} \cdot (\vec{\sigma} \times \vec{\nabla} V), \quad (12)$$

where $\vec{\nabla} V$ is the electric field generated by an effective potential due to not only all of the other electrons in the solid, but also the nuclear cores, and $\vec{\sigma}$ is the Pauli spin operator. The spin-orbit interaction H_{SO} couples the spin-up and spin-down states and doubles the size of the Hamiltonian matrix from that of the scalar-relativistic one-spin Hamiltonian matrix. In addition, the spin-orbit interaction couples the orbital angular momentum of the electron to its own spin magnetic moment, and causes a reduction in the symmetry of the crystal. Magneto-optical effects also depend upon exchange effects accounting for the splitting of the degeneracy of spin-up and spin-down states. Erskine and Stern¹⁶ showed how the spin-orbit interaction and exchange splitting affect the absorptive part of the off-diagonal conductivity by using an atomic picture, while Misemer¹⁵ demonstrated this in a band picture. Note that in Eq. (9), there may be extensive cancellation of terms with opposite signs, and $|\sigma_{xy}|$ is typically of the order of 1% of $|\sigma_{xx}|$. Thus σ_{xy} can be a more sensitive test of the electronic structure than σ_{xx} .

IV. RESULTS AND DISCUSSION

The measured absorptive parts of the diagonal optical conductivity (σ_{1xx}) for RFe_2 ($R = \text{Gd, Tb, Ho, Lu}$) and GdCo_2 are shown in Fig. 1. Broad peaks were found between 2.0 and 3.0 eV for these compounds. Sharipov *et al.*¹⁷ obtained a similar broad peak between 2.0 and 3.0 eV in the

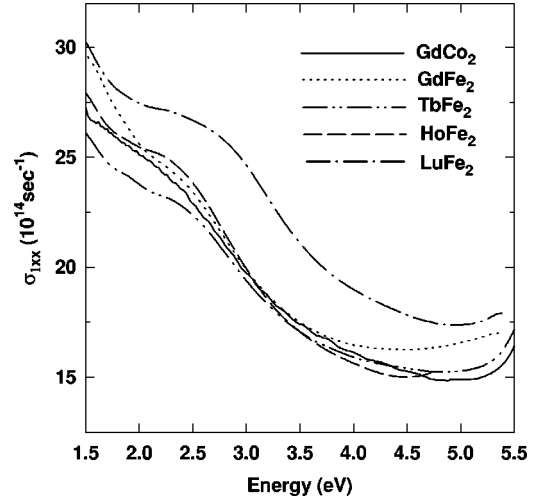


FIG. 1. Optical frequency dependency of the real parts of the diagonal optical conductivity for HoFe_2 , TbFe_2 , GdFe_2 , GdCo_2 , and LuFe_2 , measured at room temperature.

real part of the diagonal optical conductivity for polycrystalline GdFe_2 .

Because the experiment has been conducted in air, oxidation on the surfaces of the samples cannot be avoided. Many authors^{18–21} used a three-phase model to study the effect of oxidation on Si and GaAs. Gd and Fe or Co in GdFe_2 and GdCo_2 oxidize readily. Gd_2O_3 , FeO , Fe_3O_4 , and Fe_2O_3 are known, as is GdFeO_3 . The surface oxide need not be any of these, but could be an amorphous oxide. A correction can be made if the thickness and refractive index of the overlayer are known. A more serious problem is disproportionate oxidation of one of the two metallic elements, for that would leave Fe- or Gd-rich regions in the oxide layer or at its interface with the underlying metal, and these regions could contribute another component to the off-diagonal optical conductivity spectra. It appears that the growth of oxide layers on GdFe_2 and GdCo_2 is self-limiting, since the changes in ellipsometric spectra taken on a growth surface days, weeks and months after preparation decrease with time. However, Lee and Choudhury²² have shown that in GdCo_2 , Co precipitates in the oxide, especially if the sample is heat treated.

We have studied the oxide layers of GdFe_2 and GdCo_2 by Auger spectroscopy, secondary-ion mass spectroscopy, and x-ray induced photoemission, all as a function of sputtering time with Ar or Ne ions. The three techniques agree that the composition of the oxide is reasonably homogeneous throughout its depth and that the underlying compound is similarly homogeneous with depth. However, the Co x-ray photoemission spectroscopy spectra show a peak shift with increasing depth in the oxide indicative of more metallic binding; Co precipitates may be present. The sputter times to the interface led to an estimate of 200–500 Å for the oxide thickness. Multiple-angle ellipsometry led to an oxide thickness estimate of 300–400 Å for LuFe_2 and GdFe_2 if the oxide refractive index is assumed to be that of SiO_2 .²³ For the study of the effects of oxidation on the off-diagonal optical conductivity, Chen *et al.*'s general expression for the magneto-optical polar Kerr effect in a bilayer system^{24,25} was employed by treating the oxide layer on $R\text{Co}_2$ as a transpar-

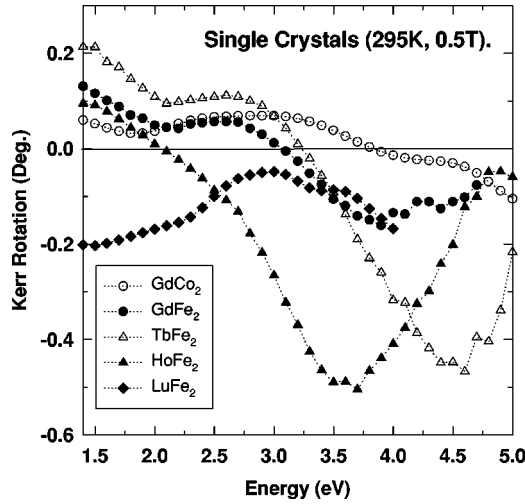


FIG. 2. Kerr rotations of single crystals of GdCo_2 and RFe_2 ($R=\text{Gd}, \text{Tb}, \text{Ho}, \text{Lu}$) measured at room temperature with an applied magnetic field of approximately 0.5 T.

ent dielectric with an effective refractive index and thickness. Corrections for several assumed thicknesses of oxide overlayer on GdCo_2 have been made,²⁶ assuming the refractive index of the oxide is that of SiO_2 . The corrections increase the magnitude of σ_{1xx} , but do not alter the structures appreciably. However, in σ_{2xy} the positions of peaks shift upon correction, accompanied by changes in the magnitude; the relative changes are more significant than in σ_{1xx} .

Figures 2 and 3 show the Kerr rotation and ellipticity measured at room temperature using a $\text{NdFe}_2\text{B}_{14}$ permanent magnet with a magnetic field of approximately 0.5 T. As shown in Figs. 3 and 4, the MOKE spectra are quite diverse. The peak positions of the Kerr rotation and ellipticity are noticeably shifted from each other and fine features are also observed. For LuFe_2 , the sign of the Kerr rotation and ellipticity is negative while those of the others cross from positive to negative. This is described in detail in the summary and conclusions. At room temperature, an applied field of 0.5 T yields about 90% magnetic saturation for

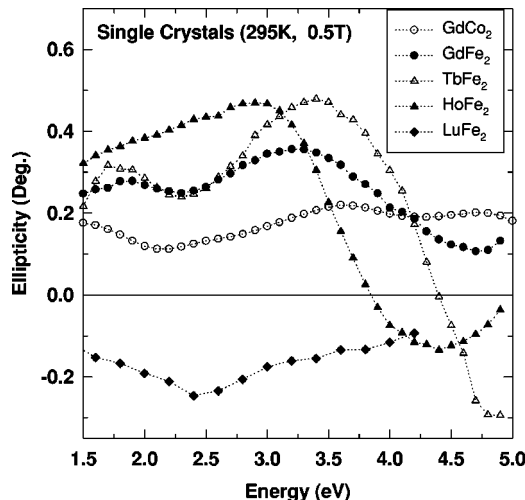


FIG. 3. Ellipticities of single crystals of GdCo_2 and RFe_2 ($R=\text{Gd}, \text{Tb}, \text{Ho}, \text{Lu}$) measured at room temperature with an applied magnetic field of approximately 0.5 T.

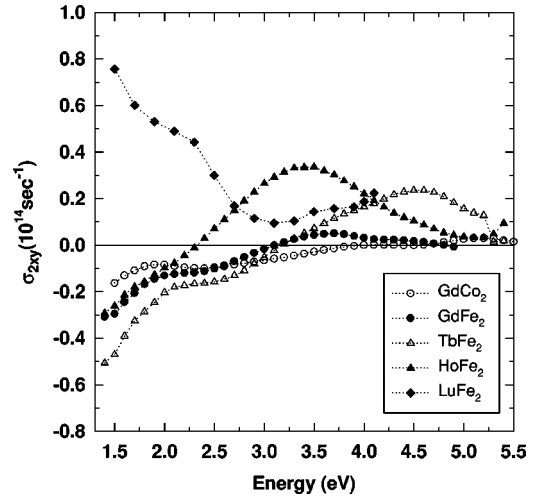


FIG. 4. Optical frequency dependency of the imaginary parts of the off-diagonal optical conductivity component calculated using the room-temperature MOKE data shown in Figs. 2 and 3. The applied magnetic field was 0.5 T.

GdFe_2 , GdCo_2 , LuFe_2 and about 70% for TbFe_2 and HoFe_2 from the superconducting quantum interference device measurements. At room temperature, they are all ferromagnetic with Curie temperatures between 600 and 800 K. These data contain no effects of Faraday rotation or strain induced birefringence. The absorptive parts of the off-diagonal optical conductivity (σ_{2xy}) for these compounds are shown in Fig. 4. The magnitude of σ_{1xx} is much larger than that of σ_{2xy} . The sign of σ_{1xx} is always positive while that of σ_{2xy} can be both positive and negative as shown in Fig. 1. The similar broad peaks in σ_{1xx} are shifted away from each other in the case of σ_{2xy} as shown in Fig. 4. The Kerr rotations of single-crystal and polycrystalline GdFe_2 , measured at different temperatures and magnetic fields, are shown in Fig. 5. The solid squares and the solid circles represent the Kerr rotations of single-crystal GdFe_2 measured at room temperature with an applied magnetic field of about 0.5 T and measured at 7 K with an applied magnetic field of 1.4 T. The Kerr rotation of single crystal GdFe_2 measured at higher magnetic field and lower temperature shows clearer features and a larger magnitude as expected. As shown in Fig. 6, the magnetic moment of single-crystal GdFe_2 is fully saturated with an applied magnetic field of 1.4 T at 5 K. We made polycrystalline GdFe_2 by arc melting and polished it mechanically for the optical measurements. The Kerr rotation of a single crystal of GdFe_2 crosses from positive to negative at 3.1 eV while that of polycrystalline GdFe_2 remains positive.

The Kerr rotation measured out of the cryostat at room temperature with an applied magnetic field of 0.5 T has no Faraday rotation due to the windows and no-strain induced birefringence due to differential thermal expansion or pressure differential on the windows. Kerr rotations measured inside the cryostat and outside of the cryostat cross zero at the same energy, 3.1 eV, as shown in Fig. 5. This means that the shift of the Kerr rotation due to strain or Faraday rotation measured inside the cryostat is negligible, i.e., the corrections were adequate. The Kerr rotation measured inside the cryostat has a maximum value of about 0.3° at 1.5 eV and a

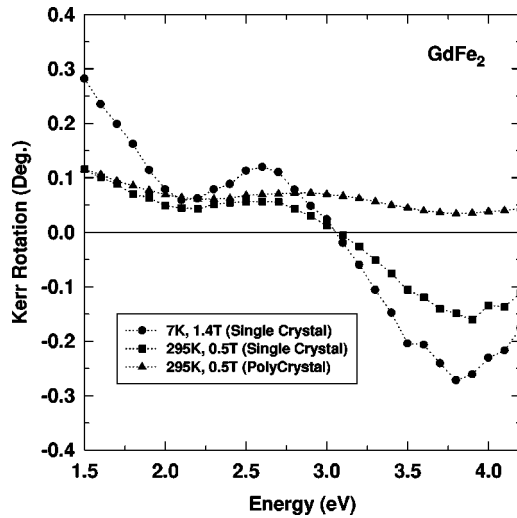


FIG. 5. Kerr rotations of single-crystal and polycrystalline GdFe_2 measured at 7 and 295 K with applied magnetic fields of 1.4 and 0.5 T.

minimum value of about -0.3° at 3.8 eV, crossing zero at 3.1 eV, while the Kerr rotation measured out of the cryostat has a maximum value of about 0.12° at 1.5 eV and a minimum value of about -0.15° at 3.9 eV, crossing zero at 3.1 eV. From these comparisons between measurements inside and outside the cryostat, one can see very similar features: the magnitudes of the Kerr rotation are different due to different magnitudes of the magnetic fields.

Figure 7 shows the Kerr rotations and ellipticities of single-crystal and polycrystal TbFe_2 measured at different temperatures and applied magnetic fields. The peak negative Kerr rotation appeared around 4.6 eV for both samples measured at 295 K and 0.5 T, similar to that of Katayama's polycrystalline data.¹ For polycrystalline TbFe_2 measured at 7 K and 1.26 T, the absolute magnitude of the Kerr rotation at 4.6 eV is quite similar to that of Katayama¹ measured with polycrystalline TbFe_2 at room temperature and 1.2 T. The magnitude of the Kerr rotation of the single crystal of TbFe_2 at 4.6 eV is 0.46° while that of the polycrystal of TbFe_2 is

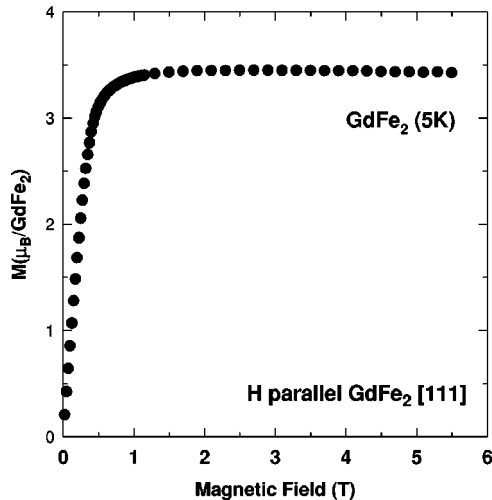


FIG. 6. Magnetization measured as a function of applied magnetic field at 5 K. The field was applied perpendicular to the plane of the specimen.

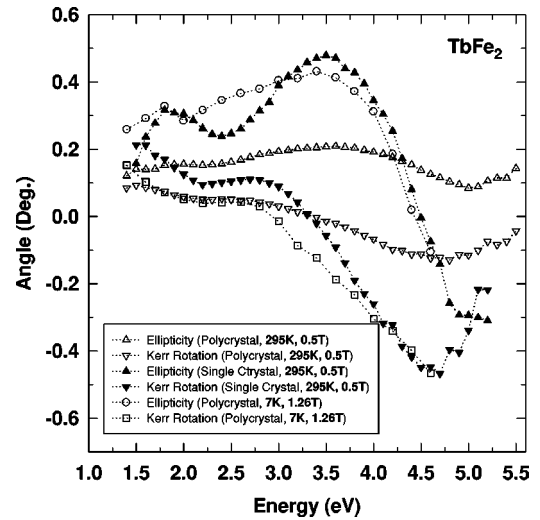


FIG. 7. Kerr rotation and ellipticity data for single-crystalline and polycrystalline TbFe_2 measured using the temperature and fields indicated in the figure.

0.12° measured under the same conditions. The Kerr rotation of the single crystal is almost four times larger than that of the polycrystalline sample. Compared to the Kerr rotation of Katayama, the magnitude and shape are quite similar in the case of the single crystal, even though we applied a smaller magnetic field. There is a small flat shoulder between 2.2 and 2.8 eV in the Kerr rotation spectrum of TbFe_2 of Ref. 1. As shown in Fig. 7, we can see also a similar feature between 2.1 and 3.0 eV, but the shoulder is more clear than that of Ref. 1. In the case of our polycrystalline sample, the Kerr rotation is smaller than that in Ref. 1, due to smaller applied magnetic field.

We found that the single-crystal TbFe_2 shows a larger Kerr rotation and more features than the polycrystal under the same experimental conditions. This result may have several causes. First, mechanical polishing of the polycrystal causes surface strain, so the magnetic domains may be more difficult to align compared to samples with unstrained surfaces. Therefore one can expect a higher magnetic field is required to achieve saturation than for an unstrained surface. To relax the strained surface, annealing the sample may be necessary. However, we found annealing the polycrystalline TbFe_2 in vacuum expedited oxidation and grain growth. The annealed surface lost its luster due to the oxidation or due to grain growth, which caused roughening. Chemical etching may dissolve one component more than the other component. The surface of the single crystal of TbFe_2 grown from the binary melt is mirrorlike, so no further surface treatments were necessary to make the surface suitable for optical measurements. Therefore no surface strain problem arose from mechanical polishing as for the polycrystal sample. The second factor which may affect the surface quality is oxidation. While polishing the surface of a polycrystalline sample with alumina solution, contact with water is unavoidable. This may expedite the rate of oxidation. It is known that higher humidity increases the oxidation rate.²⁷ Allen and Connell²⁸ found that oxidation reduces the reflectivity and the polar Kerr rotation of $\text{Tb}_x\text{Fe}_{1-x}$ ($x \approx 0.21$). Therefore MOKE data from single crystals are more likely to represent the ideal

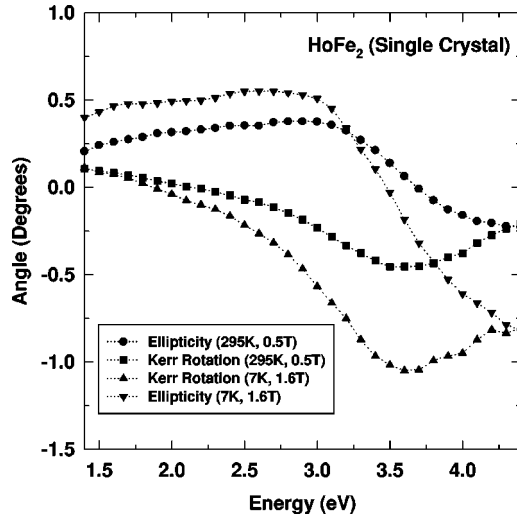


FIG. 8. Kerr rotation and ellipticity data for single-crystalline HoFe_2 measured using the temperature and fields indicated in the figure.

MOKE spectra of the magnetic materials under investigation.

We also measured Kerr rotation and ellipticity of HoFe_2 at different temperatures and different magnetic fields. Figure 8 shows the Kerr rotation and ellipticity of a single crystal of HoFe_2 measured at 7 and 295 K and 0.5 and 1.6 T, respectively. At 7 K and 1.6 T, the magnetic moment of single crystal of HoFe_2 is about 90% of the saturated magnetic moment. The negative peak position appeared at 3.7 eV for both samples. The absolute magnitude of the peak Kerr rotation of polycrystalline HoFe_2 measured¹ with an applied magnetic field of 1.2 T is only 0.17° . Compared to that, the absolute magnitude of the peak Kerr rotation of the single crystal of HoFe_2 is 1.1° , six times larger. Even with an applied magnetic field of 0.5 T, the peak Kerr rotation is larger. But the peak position for HoFe_2 reported in Ref. 1 for polycrystalline specimens is shifted to higher energy by 0.3 eV compared with our data. This difference might come from the effect of oxidation on the surface of the sample, but this needs to be studied more.

As far as we know, there has been no report on the bremsstrahlung isochromat spectroscopy (BIS) or inverse photoemission spectroscopy (IPES) spectrum of single crystals of $R\text{Fe}_2$ ($R=\text{Gd}$, Tb , and Ho). The locations of the occupied and unoccupied $4f$ levels of bulk Gd metal are -8.5 and 3.5 eV with respect to the Fermi level, respectively, from PES and IPES data.²⁹ The LSDA calculation of GdFe_2 using the TB-LMTO with spin-orbit interactions included gives the positions Gd- $4f$ occupied and unoccupied states as -3.5 and 1.3 eV with respect to the Fermi level, respectively. The difference of the occupied states between the experiment and theory based on the LSDA of Gd- $4f$ states are very large, -8.5 and -3.5 eV, respectively. The LSDA does not treat the strong correlations of the localized $4f$ electrons in GdFe_2 correctly. The theoretical σ_{2xy} of $R\text{Fe}_2$ ($R=\text{Gd}$, Tb , and Ho) using the TB-LMTO based on the LSDA are not in agreement with the experimental σ_{2xy} , both in magnitude and spectral shapes due to the incorrect electronic structures which lead to the wrong interband transitions.¹⁰ Figure 9 shows the comparison for the experimental and theoretical

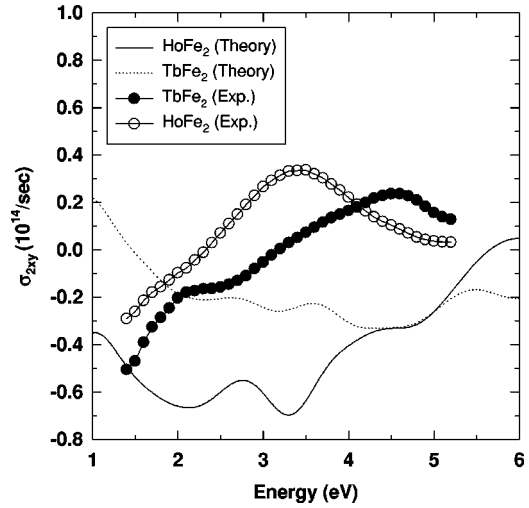


FIG. 9. Comparison of measured and calculated absorptive part of the off-diagonal optical conductivities (σ_{2xy}) for TbFe_2 and HoFe_2 . A lifetime broadening of 0.5 eV was used and no Drude contribution was included in the theoretical results.

absorptive part of off-diagonal optical conductivity for HoFe_2 and TbFe_2 between theory and experiment. The peak positions and shapes of the experiment spectra do not agree with the results obtained from the TB-LMTO method. Compared to the poor agreement between theory and experiment for $R\text{Fe}_2$ whose $4f$ shell is open, the magneto-optic spectra of LuFe_2 whose $4f$ shell is closed agreed well with theoretical spectra obtained using the TB-LMTO scheme. Figure 10 shows the experimental and theoretical values of the absorptive part of the off-diagonal optical conductivity (σ_{2xy}) of LuFe_2 . The theoretical σ_{2xy} was obtained from Eq. (9). For compounds containing rare earths with a partially filled $4f$ shell the localized $4f$ states cannot be adequately treated with the LSDA, and the so-called LSDA+ U method, which explicitly includes the on-site Coulomb interaction among

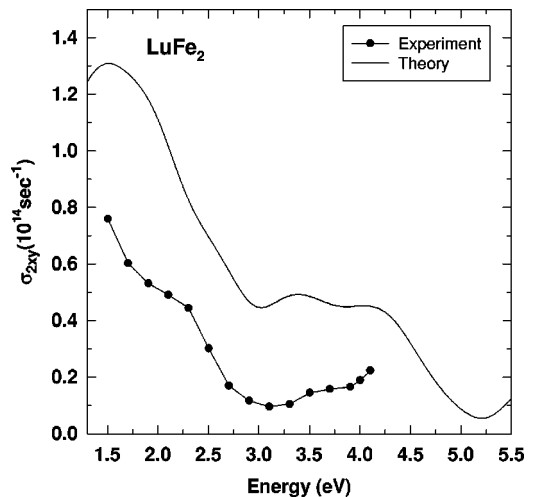


FIG. 10. Comparison of measured and calculated absorptive part of the off-diagonal optical conductivities (σ_{2xy}) of LuFe_2 . Theoretical values determined from TB-LMTO (solid lines) and experimental results obtained from ellipsometry and Kerr spectroscopy (dotted lines). A lifetime broadening of 0.4 eV was used and no Drude contribution was included in the theoretical results.

highly correlated localized electrons, seems to offer the possibility of an improved description of the magneto-optic spectra.³⁰

V. SUMMARY AND CONCLUSIONS

We have grown single crystals of rare-earth transition (RT) intermetallic compounds. We have measured the optical constants of these samples using a spectroscopic ellipsometer. By combining the magneto-optical parameters (Kerr rotation and ellipticity) and the optical constants, we obtained the off-diagonal optical conductivity at room temperature.

The absorptive parts of the optical conductivities (σ_{1xx}) of RFe_2 ($R = \text{Ho, Tb, Gd, and Lu}$) and $GdCo_2$, Fig. 1, have very similar features, broad peaks between 2.0 and 3.25 eV. Ellipsometry shows little differences due to the different number of $4f$ electrons in the RT_2 compounds and the different magnetic properties of these materials.

The absorptive part of the off-diagonal optical conductivity (σ_{2xy}) can be compared directly with the theoretical σ_{2xy} obtained from electronic structure calculations of the magnetic materials. In the case of $LuFe_2$ in which the $4f$ states are fully occupied, the theoretical and experimental values of magneto-optical parameters and off-diagonal optical conductivity agree well with each other.³¹ But for other RFe_2 and $GdCo_2$, where the $4f$ states are not fully occupied, the $4f$ electrons are actively involved in the magnetic properties and electronic properties of the samples and the LSDA approach did not give good results.

Compared to the spectrum of σ_{1xx} , the spectrum of σ_{2xy} (Fig. 4) shows quite diverse features. First, σ_{2xy} of $LuFe_2$ is positive at low energies while those of the other samples are negative. This can be explained from the magnetic properties of these compounds. In $LuFe_2$, the magnetic moments are dominated by Fe because the $4f$ states of Lu are fully occupied. Therefore the magnetic moments of Fe are aligned parallel to the applied external magnetic field. The magnetic moments of the other RFe_2 samples are dominated by rare earths and the Fe moments align opposite to the applied field. This means the Kerr rotation in RFe_2 contributed by the Fe character is opposite in sign to that of elemental Fe and $LuFe_2$ due to the ferrimagnetic properties of RFe_2 .

Second, the magnitude of the MOKE of $GdFe_2$ is larger than that of $GdCo_2$, as shown in Figs. 1–3. It may be due to the weaker exchange splitting of Co. The different features in σ_{2xy} , Kerr rotation, and ellipticity of $GdFe_2$ and $GdCo_2$ arise from different exchange splitting and different strengths of the hybridization between Gd and Fe or Co.

Third, the positions of the broad peaks in σ_{2xy} in $HoFe_2$, $TbFe_2$, and $GdFe_2$ are different (Fig. 4). In the case of σ_{1xx} , the peaks are located around 2.5 eV. But in σ_{2xy} , the peaks located in the higher energy region are between 3.2 and 4.5 eV. The different peak positions among $GdFe_2$, $HoFe_2$, and $TbFe_2$ could be caused by different positions of the occupied and unoccupied $4f$ states of the rare earths relative to the Fermi energy.

Because Fe is the common element in RFe_2 compounds, the different features of σ_{2xy} related to MOKE are related to the different magnitudes of the spin-orbit coupling and exchange splitting of rare earths and hybridization between the rare earth bands and the Fe bands. The Fe- $3d$ spin-orbit interaction is common to all RFe_2 . It is much smaller than that of $R-4f$ and $R-5d$. Therefore it may not be an important factor in generating different magnitudes of σ_{2xy} among the RFe_2 series. The different electronic structures caused by the different hybridization between the rare earth bands and the Fe bands may play a role in producing different features of σ_{2xy} in RFe_2 series. One should notice that the MOKE is dependent not only on the spin-orbit interaction itself but also on the joint density of states and the dipole matrix elements.¹⁵

Katayama¹ argued that the absolute magnitudes of the peak Kerr rotations in RFe_2 decrease with increasing $4f$ electron count and the absolute magnitude of the peak Kerr rotation of $TbFe_2$ is two times larger than that of $HoFe_2$. Their measurements are contrary to the fact that the MOKE has a linear dependence on the strength of the spin-orbit interaction when other physical parameters are fixed.¹⁵ The spin-orbit splitting Δ_{so} increases as the number of $4f$ electrons increases in rare earths.³² Therefore the spin-orbit interaction of $4f$ states of Ho in $HoFe_2$ is larger than that of Tb in $TbFe_2$. Thus we expect MOKE to be larger in $HoFe_2$ than in $TbFe_2$. As shown in Fig. 4, the magnitude of the peak of σ_{2xy} of $HoFe_2$ is larger than that of $TbFe_2$. The magnitude of the Kerr rotation of $HoFe_2$ measured at 295 K in 0.5 T is similar to that of $TbFe_2$ shown in Fig. 2, unlike the measurement of Katayama. The difference may arise because the differences between polycrystalline and single-crystal samples. It is clear that MOKE measurements are better carried out using single-crystalline specimens.

ACKNOWLEDGMENTS

Ames Laboratory is operated for the U.S. Department of Energy by Iowa State University under Contract No. W-7405-Eng-82. This work was supported by the Director for Energy Research, Office of Basic Energy Science.

¹T. Katayama and K. Hasegawa (unpublished).

²K.M. Mukimov, Sh.M. Sharipov, and L.A. Ernazarova, *Phys. Status Solidi B* **127**, K129 (1985).

³*Binary Alloy Phase Diagrams*, 2nd ed., edited by T. B. Massalski (The Materials Information Society, Materials Park, OH, 1992).

⁴P.C. Canfield and Z. Fisk, *Philos. Mag. B* **65**, 1117 (1992).

⁵D.E. Aspnes and A.A. Studna, *Appl. Opt.* **14**, 220 (1975).

⁶R.M.A. Azzam and N.M. Bashara, *Ellipsometry and Polarized*

Light (North-Holland, Amsterdam, 1977).

⁷E.A. Stern, J.C. McGroddy, and W.E. Harte, *Phys. Rev.* **135**, A1306 (1964).

⁸K. Sato, *Jpn. J. Appl. Phys.* **20**, 2403 (1981).

⁹K. Sato, H. Hongu, H. Ikekame, Y. Tosaka, M. Watanabe, K. Takanashi, and H. Fujimori, *Jpn. J. Appl. Phys., Part 1* **32**, 989 (1993).

¹⁰S.J. Lee, Ph.D. thesis, Iowa State University, 1998.

- ¹¹X.D. Wang, Ph.D. thesis, Iowa State University, 1994.
- ¹²O.K. Andersen, Phys. Rev. B **12**, 3060 (1975).
- ¹³U. von Barth and L. Hedin, J. Phys. C **5**, 1629 (1972).
- ¹⁴R. Kubo, J. Phys. Soc. Jpn. **12**, 570 (1957).
- ¹⁵D.K. Misemer, J. Magn. Magn. Mater. **72**, 267 (1988).
- ¹⁶J.L. Erskine and E.A. Stern, Phys. Rev. B **8**, 1239 (1973).
- ¹⁷Sh.M. Sharipov, K.M. Mukimov, L.A. Ernazarova, A.V. Andreyev, and N.V. Kuorevatykh, Phys. Met. Metallogr. **69**, 50 (1990).
- ¹⁸E.A. Irene, Thin Solid Films **233**, 96 (1993).
- ¹⁹T.D. Burleigh, S. Wagner, and T.F. Ciszek, Sol. Cells **13**, 179 (1984).
- ²⁰P.J. McMarr, K. Vedom, and J. Narayan, J. Appl. Phys. **59**, 694 (1986).
- ²¹U. Rossow, in *Linear and Nonlinear Optical Spectroscopy of Surfaces and Interfaces*, edited by J.F. McGilp, D. Weaire, and C. H. Patterson (Springer-Verlag, Berlin, 1995), Chap. 3, p. 53.
- ²²E.W. Lee and G.M. Choudhury, J. Less-Common Met. **46**, 305 (1976).
- ²³S.J. Lee, S. Zollner, P.C. Canfield, and D.W. Lynch (unpublished).
- ²⁴L.Y. Chen, W.A. McGahan, Z.S. Shan, D.J. Sellmyer, and J.A. Woollam, J. Appl. Phys. **67**, 5337 (1990).
- ²⁵L.Y. Chen, W.A. McGahan, Z.S. Shan, D.J. Sellmyer, and J.A. Woollam, J. Appl. Phys. **67**, 7547 (1990).
- ²⁶S. J. Lee, K. J. Kim, P. C. Canfield, and D. W. Lynch, J. Magn. Magn. Mater. (to be published).
- ²⁷K. A. Gschneidner, Jr., *Specialty Inorganic Chemicals* (The Royal Society of Chemistry, London, 1981).
- ²⁸R. Allen and G.A.N. Connell, J. Appl. Phys. **53**, 2353 (1982).
- ²⁹F. Gerken, A.S. Flodström, J. Barth, and C. Kunz, Phys. Scr. **32**, 43 (1985).
- ³⁰B.N. Harmon, V.P. Antropov, A.I. Liechtenstein, I.V. Solov'yev, and V.I. Ansimov, J. Phys. Chem. Solids **56**, 1521 (1995).
- ³¹S.J. Lee, R. Lange, S. Hong, S. Zollner, P.C. Canfield, B.N. Harmon, and D.W. Lynch, Thin Solid Films **313-314**, 222 (1998).
- ³²B.I. Min, and Y.-R. Jang, J. Phys.: Condens. Matter **3**, 5131 (1991).